AGU PUBLICATIONS

JGR

Journal of Geophysical Research: Oceans

RESEARCH ARTICLE

10.1002/2016JC012498

Key Points:
- The vertical structure of currents is needed for estimating of surface gravity wave steepness from our buoy measurements
- Waves are limited by a bulk, finite depth steepness parameter. Models based on this steepness fit the observed breaking
- A quasi-spectral model does well to describe the measured wave breaking. The influence of directional spread is discussed

Correspondence to:
S. Zippel,
zippelsf@uw.edu

Citation:
Zippel, S., and J. Thomson (2017), Surface wave breaking over sheared currents: Observations from the Mouth of the Columbia River, *J. Geophys. Res. Oceans*, *122*, doi:10.1002/2016JC012498.

Received 22 OCT 2016
Accepted 14 MAR 2017
Accepted article online 17 MAR 2017

Surface wave breaking over sheared currents: Observations from the Mouth of the Columbia River

Seth Zippel[1] and Jim Thomson[1]

[1]Applied Physics Lab, University of Washington, Seattle, Washington, USA

Abstract Measurements of waves and currents from freely drifting buoys are used to evaluate wave breaking parameterizations at the Mouth of the Columbia River, where breaking occurs in intermediate depths and in the presence of vertically sheared currents. Breaking waves are identified using images collected with cameras onboard the buoys, and the breaking activity is well-correlated with wave steepness. Vertical shear in the currents produces a frequency-dependent effective current that modifies the linear dispersion relation. Accounting for these sheared currents in the wavenumber spectrum is essential in calculating the correct wave steepness; without this, wave steepness can be over (under) estimated on opposing (following) currents by up to 20%. The observed bulk steepness values suggest a limiting value of 0.4. The observed fraction of breaking waves is in good agreement with several existing models, each based on wave steepness. Further, a semispectral model designed for all depth regimes also compares favorably with measured breaking fractions. In this model, the majority of wave breaking is predicted to occur in the higher frequency bands (i.e., short waves). There is a residual dependence on directional spreading, in which wave breaking decreases with increasing directional spread.

Plain Language Summary We measured wave breaking and currents at the Columbia River Mouth, the second largest river in the U.S. Breaking waves here and at other river inlets are a hazard to marine traffic, such as fishing, shipping, and boating. Rivers also bring pollutants and nutrients to the ocean, and breaking waves can influence whether they stay near the coast or travel farther out to sea. Predicting when and where waves break is difficult, especially at river inlets where tides and river currents modify the waves from how we understand them in the open ocean or at beaches. We found that currents below the surface were important in predicting where waves break. Once we accounted for these currents, wave breaking was well predicted by existing theories. These theories had yet to be extensively tested with field data from regions with strong currents, or at water depths shallower than those found in the open ocean but deeper than those found at the beach.

1. Introduction

Wave breaking and wave-current interaction at tidal and river inlets has been historically difficult to predict and understand. The effect of currents on waves is commonly smaller than the effect of bathymetry on waves, and this makes measurements of wave-current effects in the field difficult to discern from changes in tidal elevation [*Kang and Iorio*, 2006; *Olabarrietta et al*., 2011, 2014; *Mendez et al*., 2015; *Chen et al*., 2015]. Despite being a secondary effect, understanding and incorporating the effects of currents on waves is important to understand river inlet systems. For example, *Olabarrieta et al*. [2014] modeled a simplified river inlet system, showing that jet instability was increased due to the interaction of large waves with high outflow. In another study at a lagoon in Portugal, *Dodet et al*. [2013] showed enhancement of wave heights and wave dissipations on ebbs, as well as a reduction of wave heights on floods as a result of wave-current interactions. Further, *Dodet et al*. [2013] noted that incorporating wave-current feedback in model simulations added an ebb/flood asymmetry that decreased seaward transport of sediment in the tidal channel on ebbs.

Farther from the coast, refraction of waves by currents can affect how and which waves propagate to inlets. *Hopkins et al*. [2015] used models and measurements at Katama Inlet on Martha's Vineyard to show that wave refraction by currents is important for accurate prediction of waves offshore of the surf zone. *Pearman* *et al.* [2014] showed strong refraction and steepening of wind waves in drifter measurements at the San Francisco Bight. In a separate study of the San Francisco ebb tidal delta, *Hansen et al.* [2014] showed wave refraction (in this case due to a combination of bathymetry and currents) created large along shore pressure gradients offshore of the surf zone.

Wave/current effects in deep water can potentially effect buoyant plumes, as wave breaking has been suggested as a mechanism for enhanced river plume mixing. *Gerbi et al.* [2013] modeled a buoyant river plume during upwelling-favorable winds, finding the plume was thicker when a wave breaking turbulence parameterization was included. *Thomson et al.* [2014] showed near surface turbulent kinetic energy dissipations due to wave breaking at a front formed by the Columbia River plume were larger when short waves were present, possibly causing a thicker plume than was observed on an adjacent day without short waves.

While currents affect waves through refraction and steepening, wave breaking has an effect on currents through turbulence injection into the ocean surface [*Craig and Banner*, 1994; *Terray et al.*, 1996], and through wave-breaking-induced radiation stress gradients [*Longuet-Higgins and Stewart*, 1962]. Therefore, better understanding of wave breaking at river inlets can lead to improvements in prediction of not only the waves themselves, but of currents, water quality, and sediment transport.

Wave breaking also poses a hazard to marine traffic. River inlets are often both active areas for vessels, and dangerous to navigate [*Masson*, 1996]. Improved understanding of wave breaking at sites with strong currents could help improve safety in these complex, highly trafficked areas.

1.1. Wave-Breaking Models

Wave breaking is often separated into two regimes based on the ratio of depth d and wavelength L: (1) deep water, where the ratio of depth to wavelength is $d/L > 1/2$ and (2) shallow water, where $d/L < 1/20$. Breaking at river inlets often occurs in intermediate depths, and therefore models developed to include the effects of currents are often modified from either regime. However, because the deep and shallow models were developed separately, the wave-current breaking schemes often have fundamentally different approaches. Shallow models [e.g., *Battjes and Janssen*, 1978; *Thornton and Guza*, 1983] explicitly define breaking fraction from a probabilistic assumption of breaking wave heights. In contrast, deep models [e.g., *van der Westhuysen*, 2012] often skip explicit definition of breaking fraction in favor of direct estimates of wave dissipation modified from white capping or saturation models. As a result, these latter models will be discussed, but not directly compared with data in this study.

Battjes and Janssen [1978] developed one of the first wave-breaking models for the surf zone. They combined the steepness limit from *Miche* [1944], and the assumption that all waves with heights above this steepness limit in a Rayleigh distribution were breaking (i.e., a clipped wave height distribution), leading to a transcendental equation for breaking fraction

$$\frac{1-Q_b}{\ln(Q_b)} = -\left(\frac{H_{rms}}{H_{\max}}\right)^2, \tag{1}$$

where Q_b is the fraction of breaking waves to the total number of waves and H_{rms} is the root mean square wave height. Using an approximation for the *Miche* [1944] steepness limit (as described in *Chawla and Kirby* [2002]), $H_{\max}k_m/\tanh(k_m d) = \gamma$, the equation above can be restated as

$$\frac{1-Q_{b,BJ78}}{\ln(Q_{b,BJ78})} = -\left(\frac{H_{rms}k_m}{\gamma\,\tanh(k_m d)}\right)^2, \tag{2}$$

where k_m is the mean wavenumber, d is the water depth, and γ is a constant prescribing the breaking limit. In this form, the breaking model is more easily applied to breaking waves outside of shallow water, although only a slight modification to the breaking limit (and not the clipped Rayleigh model) was made. This form of the breaking model is also more easily applied to breaking in the presence of currents, which alter the wavenumber k (see next section).

Thornton and Guza [1983] measured breaking wave heights in the surf zone, finding broken wave height distributions did not fit the assumptions of the clipped *Battjes and Janssen* [1978] model, but rather a range of broken wave heights existed, some much less than the steepness limit. Therefore, they suggested a heuristic breaking wave height distribution function by multiplying the Rayleigh distributed wave heights by a weighting function. *Chawla and Kirby* [2002] modified this function for breaking in intermediate depth with currents,

$$W(H)=a\left(\frac{H_{rms}k_m}{\gamma\tanh(k_m d)}\right)^n\left\{1-\exp\left[-\left(\frac{Hk_m}{\gamma\tanh(k_m d)}\right)^2\right]\right\}, \tag{3}$$

where $W(H)$ is the weighting function, and $n=2$ and $a=1$ are constants. Breaking fraction can be found through integration of the breaking wave height distribution

$$Q_{b,CK02}=\int_0^\infty W(H)P(H)\mathrm{d}H=\left(\frac{H_{rms}k_m}{\gamma\tanh(k_m d)}\right)^4\left[\left(\frac{H_{rms}k_m}{\gamma\tanh(k_m d)}\right)^2-1\right]^{-1}, \tag{4}$$

where $P(H)$ is the Rayleigh distribution as a function of wave height, H. For the purposes of this study, evaluations of the wave-breaking models will be done using H_s instead of H_{rms}, which results in an increase in γ by $\sqrt{2}$.

While deep water studies of wave breaking have often favored breaking metrics besides Q_b, (i.e., focused on whitecap coverage [*Monahan*, 1971; *Monahan and Muircheartajgh*, 1980; *Callaghan et al*., 2008; *Schwendeman and Thomson*, 2015], and more recently the breaking crest speed distribution $\lambda(c)$ [e.g., *Gemmrich et al*., 2008; *Thomson and Jessup*, 2009; *Kleiss and Melville*, 2010]) there have also been studies of breaking fraction. *Banner et al*. [2000] examined breaking fractions for a collection of three different data sets, showing a frequency centered steepness $s=H_pk_p/2$ explained the trend of dominant wave breaking. Breaking fractions were fit to an exponential,

$$Q_{b,B00}=C_1(s-C_2)^{C_3}, \tag{5}$$

with $C_1=22.0, C_2=0.055, C_3=2.01$. This model was intended to capture the dominant breaking, and thus the scale of breaking waves was determined in estimation of Q_b, and considered for the steepness parameter s. For the purposes of this study, we extend the steepness parameter to include finite depths, and consider the exponential fit in both a mean sense ($s=H_sk_m/\tanh(k_md)$) to better compare this heuristic fit to the aforementioned breaking models, and in the dominant wave band as originally intended.

More recently, *Filipot et al*. [2010] proposed a breaking model for use in all depth regimes, combining ideas from *Chawla and Kirby* [2002] and *Banner et al*. [2000] (among others), as well as extending the probabilistic bulk model to a quasi-spectral model. The *Filipot et al*. [2010] steepness parameter is similar to the *Chawla and Kirby* [2002] steepness, and is defined:

$$\beta_r=\frac{H_r(f_c)k_r(f_c)}{\tanh(k_r(f_c)d)}, \tag{6}$$

with $H_r(f_c)$ and $k_r(f_c)$ defined below.

The wave spectrum is subdivided into four frequency bands related to the peak frequency, f_p. Bands are defined by a center frequency, f_c, at bands $f_c=[0.55, 1, 1.86, 3.45]\times f_p$, and a window width of $\delta=0.6$. Parameters for wave height, H, and wavenumber, k, in each band are found through integration of the wave energy spectrum multiplied with a Hann windowing function, G. For example, significant wave height for a given band, $H_r(f_c)$, would be:

$$H_r(f_c)=\frac{\sqrt{2}}{4}\sqrt{\int_0^\infty G_{fc}(f)E(f)df}, \tag{7}$$

where G is the window function (Hann window) which is nonzero in the band of interest, about center frequency f_c. The characteristic wavenumber is defined similarly, $k_r(f_c)=\int G_{fc}E(f)k\mathrm{d}f/\int G_{fc}E(f)\mathrm{d}f$. *Filipot et al*. [2010] estimate and remove the amplitude of nonlinear harmonics using an iterative method, as these nonlinear harmonics would result in overestimates of wave energy for frequencies above the peak.

The breaking rate for each band is found using a method similar to *Chawla and Kirby* [2002], via an integrated breaking wave height distribution. However, the parameters $a=1, n=2$ are changed from the values used in equation (3), to $a=1.5, n=4$. The new weighting function is:

$$W(H, f_c)=a\left[\frac{\beta_r}{\tilde{\beta}}\right]^2\left\{1-\exp\left[-\left(\frac{\beta}{\tilde{\beta}}\right)^n\right]\right\}, \tag{8}$$

where $\tilde{\beta}$ is the limiting steepness and $\beta=\beta(H)=kH/\tanh(kd)$. Originally, the limiting steepness is set to a fraction of the maximum linear steepness determined from an approximate stream function solution, $\tilde{\beta}=b\times\beta_{\max,lin}$, where $b=0.48$ and $\beta_{\max,lin}$ is a third-order polynomial of $\tanh(kD)$. For the purposes of this study, we simplify the parameterization to $\tilde{\beta}=0.48$.

1.2. Wave-Current Interactions

Waves propagating over a current experience a shift of $\vec{U}\cdot\vec{k}$ in absolute frequency ω. Often, the current speed, U is taken as a depth averaged current [*Booij et al.*, 1999], or a surface current, and applied uniformly to all frequencies. However, vertical shear results in a modification to the wave-current interaction, based on the vertical distribution of the currents relative to the vertical distribution of wave motion (which attenuates with depth according to wavenumber). This can be approximated in a depth-averaged sense by using an effective current U_{eff}, such that the linear dispersion relation is,

$$\omega=\sigma_{intr}+\vec{U}_{eff}(k)\cdot\vec{k}, \tag{9}$$

where ω is the absolute (fixed reference frame) frequency and $\sigma_{intr}=\sqrt{gk\tanh(kd)}$ is the wave intrinsic frequency (reference frame moving at U_{eff}). A deep water approximation for U_{eff} was first presented by *Stewart and Joy* [1974], and extended to finite depth by *Kirby and Chen* [1989]. The effective current, U_{eff}, is defined to a first order as,

$$U_{eff}(k)=\frac{2k}{\sinh(2kd)}\int_{-d}^{0}U(z)\cosh(2k[d+z])\mathrm{d}z, \tag{10}$$

where z is the depth below the sea surface. Thus, shorter waves effectively experience the surface current, while longer waves experience a weighted average of the current profile based on their length. This distinction between surface currents and the effective current for wave-current interaction is important, because measurements of waves using freely drifting buoys will be in a reference frame moving with the surface current, not the effective current.

Recent X-band radar measurements of waves have confirmed the analytic *Kirby and Chen* [1989] dispersion relation [*Lund et al.*, 2015; *Campana et al.*, 2016]. Using the radar-measured wavenumber, $\vec{k}$, and frequency, ω, the studies inverted the dispersion relation to estimate $U(z)$, and found estimated profiles compared favorably with acoustic Doppler measurements.

2. Methods

The Columbia River Mouth, located on the Washington-Oregon border, is known for large swells, strong tidal currents, and complex bathymetry. The inlet entrance is roughly 3.5 km wide, and has been engineered with two jetties at the mouth (a third jetty was also constructed inside the river mouth), and a dredged shipping channel is maintained out the west facing inlet, turning southward. Previous studies have shown strong wave-current interactions at this site, using both remote sensing data [*Gonzalez and Rosenfeld*, 1984] and model simulations [*Kassem and Ozkan-Haller*, 2012]. Field measurements of waves and wave breaking have historically been sparse.

For the present study, data were collected at the Mouth of the Columbia River between May and September 2013 using SWIFT drifters (http://www/apl.uw.edu/swift). Bathymetry (survey data originally from *Gelfenbaum et al.* [2015]), and drift tracks are shown in Figure 1. On ebb tides, drifters were released inside the inlet and recovered offshore after 3–4 h once the tide had changed to allow for safe passage across the Columbia Bar. On floods, the drifters were deployed inside the two jetties and kept within eyesight of the research vessel, or accompanying small boat. Drifters approaching shore were recovered and redeployed in deeper water to avoid beaching. Drifters were deployed in pairs, commonly staying within a few hundred meters of each other over the course of their deployments.

Offshore wave heights during the experiment were typically 1–2 m, tidal flows exceeded 3 m s^{-1} on strong ebbs, and wind speeds were typically 5–10 m s^{-1}. A summary of the deployments dates, tide stage, and general wind/wave conditions can be found in Table 1. Figure 2 shows histograms of the wave heights,

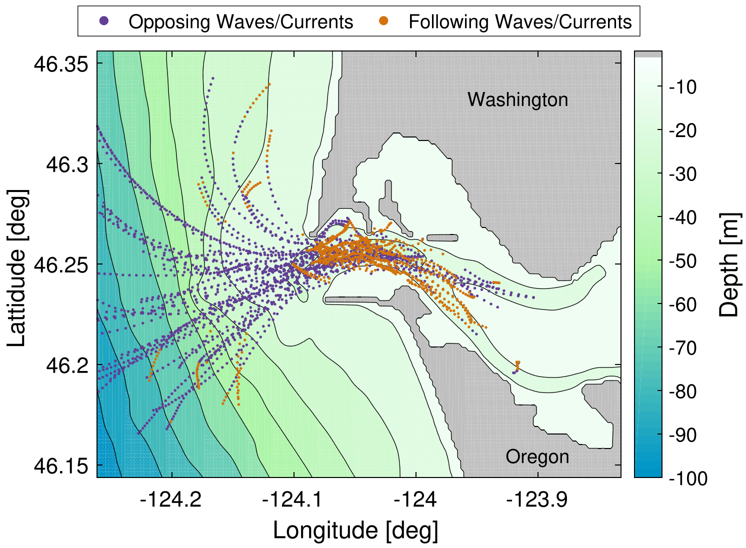

Figure 1. Centered drifter positions every 5 min are displayed over 10 m bathymetry contours at the Mouth of the Columbia River. Drifter positions are colored by the relative direction of wind and waves, purple for opposing waves and currents, and orange for following waves and currents.

peak frequencies, drift speeds, and depths measured over the course of this experiment. While opposing waves and currents generally occurred throughout ebb deployments, drifters would occasionally turn with obliquely incident waves such that there would be following relative wave/current directions when offshore. More ebbs were sampled than floods.

2.1. SWIFT Drifters

SWIFT drifters are free-floating miniature spar buoys outfitted with a suite of instruments to make measurements near the ocean surface [*Thomson*, 2012]. In this study, six second-generation SWIFTs were used, equipped to measure: wave orbital velocities, buoy drift speed, and location using a GPS logger (Qstarz BT-Q1000eX), vertical profiles of velocity using an Acoustic Doppler Current Profiler (1 MHz Nortek Aquadopp), and breaking waves using a camera (GoPro Hero2).

Clocks from each independently recording instrument were synced before each deployment. However, clock drift made exact synchronous analysis difficult. Therefore, data were processed in 5 min bursts, and averages over these bursts are used. While these short time averages result in noisy statistics, they are a compromise with the problem of statistical stationarity when drifting rapidly through a heterogeneous environment.

Table 1. Overview of Drifter Deployments

Date	Tide Stage	Winds (m s^{-1})	Wind Direction (from)	Offshore Waves (m)
21 May 13	Ebb	10	West-northwest	2.5–3.0
22 May 13	Flood to ebb	5	West-southwest	2.5–3.5
25 May 13	Ebb to flood	3–10	South	1.6
26 May 13	Ebb to flood	3–12	South-southeast	1.2
27 May 13	Slack to ebb	8–12	South	2–4
28 May 13	Ebb, then ebb to flood	5–7	Southwest	2
29 May 13	Ebb	5–10	Northwest	1.5–2.0
30 May 13	Ebb	7	South	1.5
1 Jun 13	Ebb, flood	5	South-southeast	1.0
2 Jun 13	Ebb	10	North-northwest	1.5
3 Jun 13	Flood to ebb	10	Northwest	1.5
4 Jun 13	Ebb	12–15	Northwest	1.0–1.5
6 Jun 13	Flood	3–7	Northwest	1.0–1.5
7 Jun 13	Flood	5–8	West-northwest	1.0–1.5
8 Jun 13	Ebb	5–10	North	2–3
9 Jun 13	Ebb	7.5	Northwest	2.0
22 Jul 13	Ebb and flood	5	North	1.0
23 Jul 13	Flood and ebb	5–10	North	1.2
24 Jul 13	Ebb to flood	5–8	North	1.2
25 Jul 13	Ebb to flood	5–8	North	1.2
26 Jul 13	Ebb	5–8	North	1.5
3 Sep 13	Ebb	Light		1.0
4 Sep 13	Ebb to flood	5	Southeast	0.8
8 Sep 13	Flood	10	North	1
9 Sep 13	Ebb to flood	5–8	North	1
10 Sep 13	Flood	3	North	1
11 Sep 13	Ebb to flood	8	South	1
12 Sep 13	Ebb to flood	Light		1.5
13 Sep 13	Ebb	5	West-northwest	1

[a]Offshore waves heights taken from CDIP buoy 162. Winds were measured shipboard. Tidal stage is relative to Clatsop Spit.

2.2. Currents

Drift speeds were measured using the onboard GPS logger at 5 Hz. Vertical profiles of the currents were measured with 1 MHz Doppler profilers, which were mounted internally in the spar buoy, looking down, such that the instrument head was approximately 1 m below the surface. The instrument recorded velocities in 1 m bins, up to a range of 25 m, with a 30 cm blanking distance, giving velocities

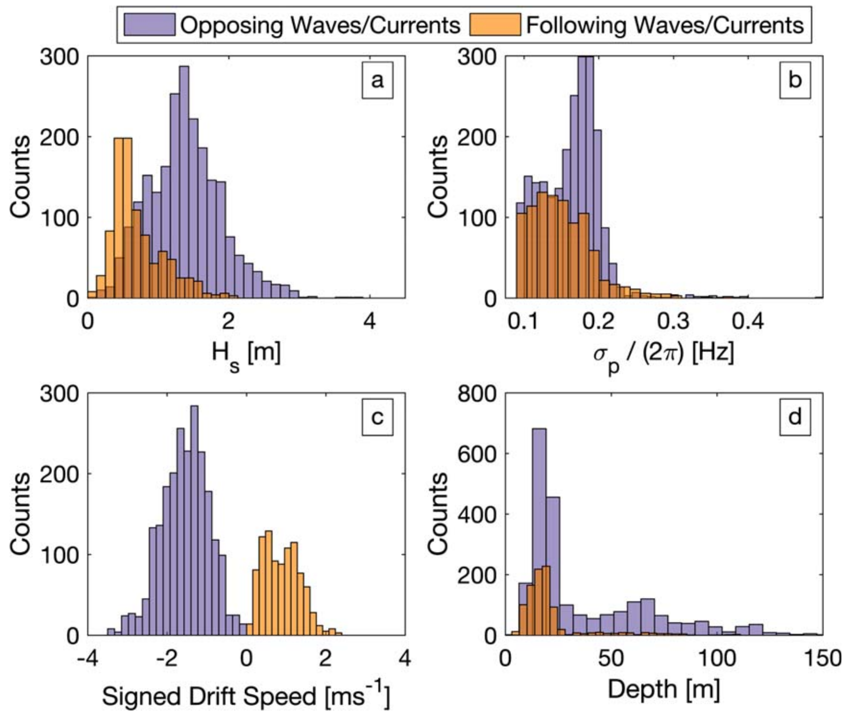

Figure 2. Histograms of (a) significant wave height, (b) peak wave frequency, (c) drift speed, and (d) depth are shown above, colored by the relative wave/current direction.

at depths ranging from 1.35 and 25.35 m below the surface. The Doppler data were recorded at 1 Hz, and averaged in 5 min intervals (300 samples per burst). Drift speeds were used to correct the measured Doppler current profiles to absolute velocities (i.e., to convert from the drifting reference frame to the fixed reference frame). Because these measurements were made from a moving platform on the free surface, they inherently include a component of the Stokes drift [*Rascle and Ardhuin*, 2009]. This Lagrangian drift component is removed before subsequent analysis. However, the Stokes drift component is relatively small when compared with the large tidal velocities, generally less than 5% of the surface drift, and less than 3% of the measured ADCP velocity.

Only two of the six drifters recorded velocity profiles, because the other four drifters were equipped with up-looking Doppler to measure surface turbulence [e.g., *Thomson et al.*, 2014]. Vertical current profiles from the two drifters were extrapolated to the other four drifters using an empirical approach, where current profiles are bin averaged by surface drift speed and direction. Appendix A expands on this process. The bin-averaged velocity profiles are shown in Figure 3. Generally, vertical shear was larger for opposing waves and currents

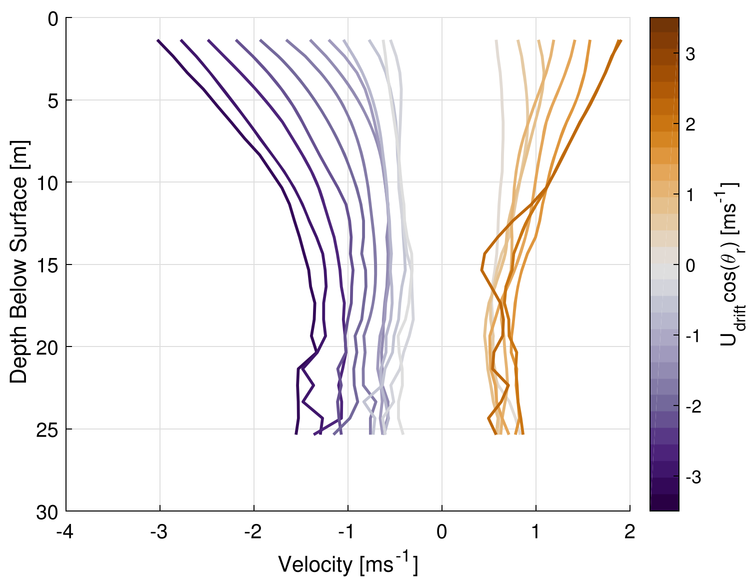

Figure 3. Profiles of velocity, bin averaged by drift speed relative to mean wave direction, are shown above. Shear was typically larger on ebbs, when waves opposed currents (purples) when compared with floods, where waves followed currents (oranges).

(primarily ebbs, purple profiles) than following waves and currents (primarily floods, orange profiles). The exception being where drifters far offshore turned to follow the dominant wind and wave direction. These data primarily fit the dark orange bin in Figure 3, where vertical shear is larger when compared to the other following wave/current profiles.

2.3. Estimating Wavenumber, *k*

Estimation of wavenumber from a moving measurement platform in the presence of vertically sheared currents requires careful attention to reference frame. Here we define three distinct reference frames, the absolute frame, ω, the wave intrinsic frame, σ_{intr}, and the measurement frame, σ_{meas}. The relation between the associated frequencies depends on the measurement platform velocity, U_{meas}, the effective velocity, $U_{eff}(k)$, and the wavenumber, which is independent of reference frame,

$$\omega = \sigma_{intr} + \vec{U}_{eff}(k) \cdot \vec{k} = \sigma_{meas} + \vec{U}_{meas} \cdot \vec{k}. \tag{11}$$

For regions of low shear or for small *k*, it is reasonable to assume that currents effects each wavenumber uniformly: $U_{meas} = U_{surface} = U_{eff}$ such that $\sigma^2_{meas} = gk\tanh(kd)$. However, in regions of large vertical shear (such as those measured during this experiment) there is significant variation from the effective current $U_{eff}(k)$ and the surface drift velocity, U_{meas}. Therefore, wavenumber must be estimated using

$$\sigma_{meas} = \sqrt{gk\tanh(kd)} - [U_{meas} - U_{eff}(k)]\cos[\theta_r(k)]k, \tag{12}$$

where we have made the assumption that the measured velocity and the effective velocity are in the same direction. Here $\theta_r(k)$ is the relative direction between the waves and the currents as a function of wavenumber.

Since estimates of U_{eff} are reliant on wavenumber (equation (10)), an iterative scheme was necessary. An initial estimate of wavenumber using the surface drift, $gk_{surf}\tanh(k_{surf}d) = \sigma^2_{meas}$ was used to estimate the first iteration of $U_{eff}(k)$ with equation (10). The resulting $U_{eff}(k)$ was used in equation (12), which was solved with MATLAB's *fminsearch* function, which employs a simplex method for finding minima in nonlinear functions [*Lagarias et al*., 1998]. This process was repeated until the percent difference in *k* when compared with the previous iteration became sufficiently small (mean percent difference less than 10^{-4}). Typically less than four iterations were required for each case (i.e., each 5 min burst average).

Figure 4a shows the change in effective current relative to the surface current based on the mean shear profiles. For frequencies above 0.4 Hz, the effect is small. However, the effect is large at low frequencies, with effective currents reaching less than 50% of the surface current. The largest relative change in effective current does not coincide with the largest currents, but rather with the largest shear. This is mostly found on ebbs, and thus the reduction from surface current to effective current is asymmetric with tide stage.

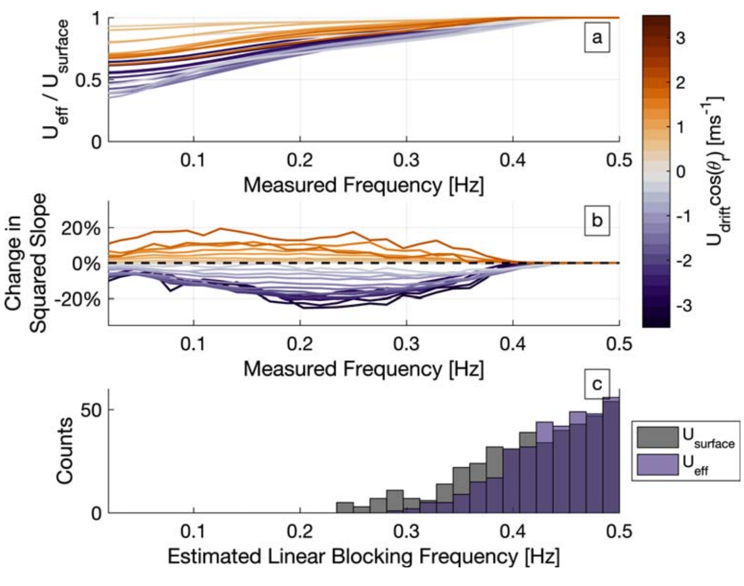

Figure 4. (a) The ratio of surface current to effective current based on the velocity profiles shown in Figure 3. (b) The percent difference in spectral squared slope, Ek^2, based on frequency and velocity profile. (c) A histogram of the estimated linear blocking frequency (the lowest frequency for which $C_g + U\cos(\theta_r) \approx 0$), using the surface current and the effective current.

Figure 4b shows the percentage change in spectral wave slope squared, which is a parameter given by Ek^2 that will be related to the analysis of wave breaking observations (to follow). The squared slope is most affected in the wind sea range, near $f_{meas} = 0.2$ Hz, despite the smallest effective currents being at low frequencies (as seen in Figure 4a). This is due to the decreasing effect of the frequency shift at low frequencies, as $\vec{U}_{eff}(k) \cdot \vec{k}$ is small when k is small. Estimated slopes are more affected by shear on opposing waves and currents, when shear is larger than on following waves and currents (floods) when vertical shear is less pronounced.

In linear theory, waves are blocked when the ambient current is equal and opposite to the intrinsic wave group speed, $C_g+U\cos(\theta_r)=0$. Using the effective current increases the frequency at which this blocking occurs, as U_{eff} is reduced relative to $U_{surface}$. A histogram of estimated blocking frequencies is shown in Figure 4c. Blocking frequency is estimated as the lowest frequency for which $C_g(f)+U\cos(\theta_r(f))=0$, although we note this estimate is sensitive to the relative direction $\theta_r(f)$. The use of U_{eff} when compared with $U_{surface}$ results in fewer blocking frequencies estimated in the 0.25–0.4 Hz range, consistent with the effects discussed in Figures 4a and 4b. For either estimate, blocking frequencies are well above the peak frequencies (Figure 2b).

2.4. Measured Wave Energy Spectra

Wave energy spectra were estimated from the 5 Hz GPS data using the *Herbers et al.* [2012] method. GPS velocity data were processed in 5 min bursts using Welch's method, where FFTs of 128 s, detrended Hanning-tapered windows were averaged with 75% overlap. Neighboring frequency bands were then merged, giving each spectrum approximately 42 degrees of freedom. Spectra of velocity, S_{uu} and S_{vv}, were converted to surface elevation spectra using:

$$E(f)=\frac{(S_{uu}+S_{vv})c^2}{g^2}, \tag{13}$$

where c is the wave phase speed. Here $c=g\tanh(kd)/\sigma$ can only be determined after obtaining the correct wavenumber at each frequency (via the iterative method in the preceding section).

Estimates of sea surface elevation from drifting platforms are sensitive to low frequency noise, as the conversion heavily weights low frequencies through multiplication by $c^2 \propto \sigma^{-2}$. There are also nonlinear interactions that affect the low frequency regions of Lagrangian measured wave spectra *Herbers and Janssen* [2016]. Here a small subset of spectra with maximum energy densities at the lowest measured frequency bins were removed from subsequent analysis. Buoy resonant motions contaminate frequencies near the natural frequency, approximately 1 Hz. Therefore, frequencies above 0.8 Hz were not considered in analysis. Further, the buoy's tilting motions result in slight overestimation of horizontal velocities in the 0.2–0.5 Hz band. An empirical frequency-dependent correction for this tilting motion was determined in a postcalibration of the buoy through the addition of an accelerometer.

Bulk wave parameters, significant wave height, H_s, mean wavenumber, k_m, and peak frequency f_p are estimated using the common forms: $H_s=4\sqrt{\int E(f)df}$, $k_m=(\int E(f)kdf)/(\int E(f)df)$, and $f_p=(\int E(f)^4 fdf)/(\int E(f)^4 df)$ [*Young*, 1999], with the integration range, $0.0625 < f < 0.8281$ Hz. Although the spectral correction for effective current is essential for the accuracy of the results that follow these bulk parameters are used to simplify much of the presentation of the results.

2.5. Wave Breaking

GoPro cameras were mounted at the top of a 1 m mast on each buoy, looking down at the ocean surface, recording images at 1 Hz. The sampling scheme resulted in approximately 12,000 images recorded per SWIFT during a single 3–4 h drift, and roughly 1.6 million images in total. Images were tagged as either breaking or nonbreaking using the method of *Rusch et al.* [2014], where each image is given a score based on four distinct analysis techniques, and high scoring images are reviewed manually to confirm breaking waves.

Image score is increased if (1) the number of relatively bright pixels in the image are above a threshold, (2) if the median of the local (3×3 pixel) range-filtered image is above a threshold, or (3) if the entropy of the image is above a threshold. These three methods give the highest score to bright, highly textured images. However, images with sun glare often have a similar brightness and texture to breaking waves, and would cause images without breaking waves to have a high score. The score of images with possible sun-glare contamination is reduced using an algorithm for the radial dependence of pixel brightness (which is strong for glare and weak for breaking waves). Because flagged images are manually reviewed, there are very few

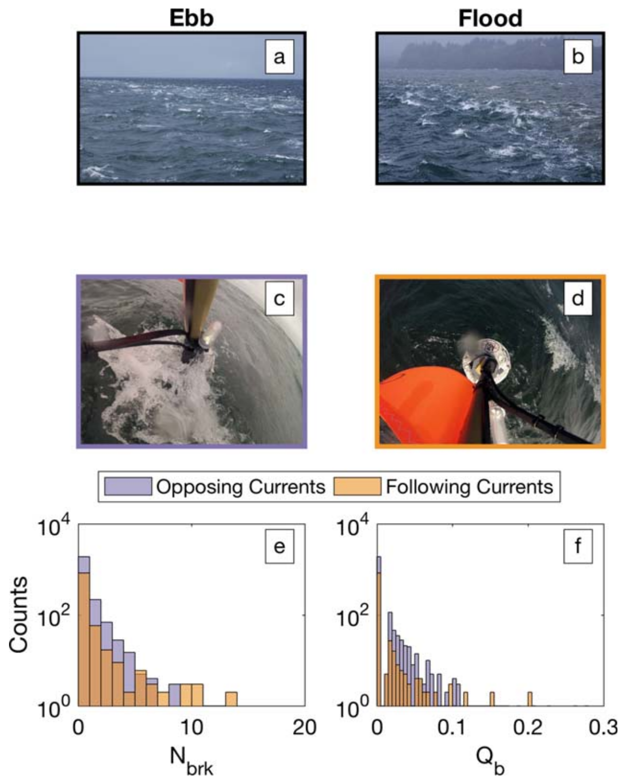

Figure 5. Examples of waves breaking on river fronts are shown for (a) an ebb example and (b) a flood example, photos courtesy of C. Bassett. Wave breaking as seen in the drifter mounted GoPro are shown in Figures 5c and 5d. Histograms of (e) breaking rates and (f) breaking fraction for all deployments, colored by opposing or following relative current direction.

images scored as breaking waves where none exist (i.e., very few false positives, or type-1 errors). However, it is likely there are breaking waves that were not flagged by the analysis (i.e., false negatives or type-2 error), and thus these estimates are likely an under prediction of the actual wave breaking.

Tilting motions from the buoy can result in large camera angles, which extend the camera footprint to the horizon and sky. Thus, images are first masked to limit the region of interest to the set of pixels near the buoy's deck. Further, a central image mask is used to exclude the pixels containing the buoy deck, mast, and flag, which can add image brightness and texture unrelated to breaking events.

The number of breaking waves in a 5 min burst, N_{brk}, is converted to breaking fraction, Q_b, using the peak wave frequency, f_p,

$$Q_b = \frac{N_{brk}}{\tau f_p}, \tag{14}$$

where $\tau = 300$ s, such that τf_p is an estimate for the number of dominant waves passing under the SWIFT during the 5 min burst. Note that this is the frequency in the drifting reference frame of the buoy ($f = \sigma_{meas}/2\pi$), because the parameter is the ratio of wave breaking to the observed waves.

Example images of breaking waves on ebb (purple) and flood (orange), as well as histograms of the total wave breaking counts, and breaking fraction are shown in Figure 5. The majority of the samples contain no breaking waves (the average breaking probability was small). Due to the short burst interval, N_{brk} has a larger effect on breaking fraction than the wave frequency. As a result, the conversion from the integer valued N_{brk} to Q_b gives a banded distribution of breaking fraction (Figures 5e and 5f).

3. Results

3.1. Limiting Bulk Steepness

Wave measurements during the experiment show a wide range of heights, lengths, and steepness values. However, all of these measurements stay below a bulk steepness limit defined by the curve,

$$\frac{H_s k_m}{\tanh(k_m d)} < 0.4, \tag{15}$$

as shown in Figure 6. This limit applies across all observations, from large swells to small wind seas. Given to the large number of measurements taken over a range of scales and conditions, this curve represents a comprehensive steepness limitation with finite-depth and shear-current effects (which are included in estimation of k via equations (10) and (12)). Here the maximum observed steepness $\gamma \approx 0.4$ is comparable to the range of limiting bulk steepness reported in previous studies, both in shallow water limit [e.g., *Raubenheimer et al.*, 1996; *Janssen and Battjes*, 2007] and deep [e.g., *Drazen et al.*, 2008; *Filipot et al.*, 2010] environments.

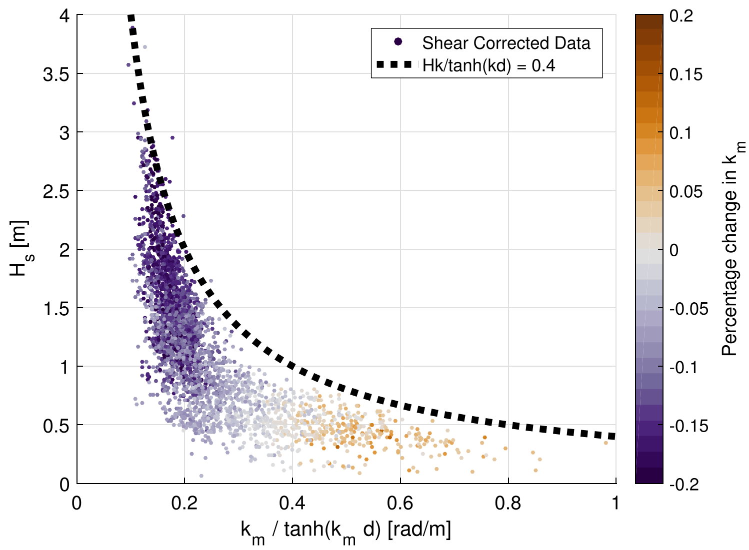

Figure 6. A scatter plot of significant wave height, H_s and depth adjusted mean wavenumber, $k_m/\tanh(k_m d)$ is shown above. Data points are colored by the percentage change in mean wavenumber from including currents relative to the surface value. Shear on opposing currents reduces the mean wavenumber (purples), and shear on following currents increases the mean wavenumber (oranges).

The importance of applying the sheared current correction in estimating wavenumber (equation (12)) is apparent here, as the majority of tall waves, $H_s > 1$ m, are measured on opposing sheared currents, and thus are up to 20% less steep than would be assumed using the surface current alone. The effect is less strong on following waves and currents, where the correction is closer to 10%. However, failure to correct the wavenumber for shear (via the effective current parameter) would obscure the universal steepness limitation shown here; instead, a spurious result of two distinct limiting steepness values would be inferred.

3.2. Breaking and the Relation to Bulk Steepness

The limiting steepness observed in the preceding section presumably occurs because of wave breaking. Indeed, Figure 7 shows that observed breaking fractions Q_b increase with bulk steepness. Three existing parametric models for wave breaking as a function of wave steepness, *Battjes and Janssen* [1978], *Banner et al*. [2000], and *Chawla and Kirby* [2002], were fit to the data by minimizing the squared residuals. The model fits are shown as curves in Figure 7, and the model fit statistics are reported in Table 2. Here we note that the *Banner et al*. [2000] model has been adjusted to use the full mean steepness, rather than the dominant steepness as originally intended, and thus a difference in the best fit constants is expected. Both the *Chawla and Kirby* [2002] and the *Banner et al*. [2000] models fit the data well. In contrast, the *Battjes and Janssen* [1978] model predicts a sharper increase in breaking with steepness than is seen in the data; it therefore under predicts breaking at low steepness values and over predicts at higher steepness values. While the *Banner et al*. [2000] model has the lowest sum of squared residuals, it has three free fitting parameters, and thus would be expected to provide a better fit. The *Chawla and Kirby* [2002] model has a similar error in using only one fit parameter, the limiting steepness γ. Further, the γ giving the best fit is similar to that used in the original study (0.84, compared to 0.96 in this study, once taking into account the difference between H_{rms} and H_s).

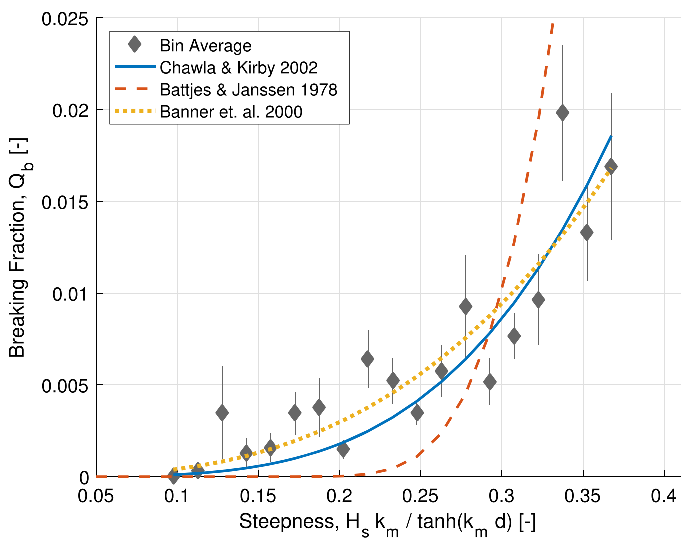

Figure 7. Breaking fractions, Q_b, are bin averaged and plotted against steepness with standard error bars in grey above. Best fits, minimizing the sum of squared residuals to the *Chawla and Kirby* [2002] (solid blue), *Battjes and Janssen* [1978] (dashed orange), and *Banner et al*. [2000] (dotted yellow) models are overlaid on the measurement averages.

Table 2. Best Fit Statistics for Bulk Wave Breaking Models

Model	Best Fit Parameters	Sum of Squared Residuals	Mean Percent Error
CK'02	$\gamma=0.96$	1.1×10^{-4}	0.4
BJ'78	$\gamma=0.65$	0.098	0.97
Ban'00 (mean)	$C_{1,2,3}=(0.29, 0, 2.8)$	9.7×10^{-5}	0.37
Ban'00 (dominant)	$C_{1,2,3}=(0.093, 0.039, 1.1)$	1×10^{-4}	0.27
Filipot'10	(not fit) $\tilde{\beta}=0.48$	XX	XX

[a]Models were best fit to minimize the sum of squared residuals to the binned means. The *Filipot et al.* [2010] model was compared to N_{meas}, and not Q_b, and is therefore not compared above.

The video data have a small geographic footprint when upright (approximately 2 m $\times$ 2 m), which potentially registers smaller wave breaking scales more easily than long breaking scales. A direct, per-scale comparison is difficult because the video data processing simply returns a binary flag for breaking on each image, and not an estimate of breaker size. However, we find the measured breaking rates increase with scale-dependent steepness as defined by *Filipot et al.* [2010] (e.g., equation (6)). Figures 8a–8c show breaking rates binned and plotted against steepness defined on different wave scales. When compared with the dominant steepness (Figure 8a), the trend appears linear, while a stronger increase of breaking rate with steepness is observed at the higher frequency bands (relative to the peak, Figures 8b and 8c). Dominant breaking fraction is also seen to increase nearly linearly with the dominant steepness (Figure 8d), and the best fit of the *Banner et al.* [2000] exponential model essentially results in a linear fit. Defining $Q_b = N_{brk}/(\tau f_c)$ introduces a slight auto-correlation with $1/f_c$ and the wave scale steepness. This auto-correlation is inverted in the previous example (e.g., Figure 7).

It is important to note that the breaking fractions measured in this study are lower than those reported in other studies, both in deep and shallow water. *Banner et al.* [2000] reports values as large as $Q_b=0.08$ in deep water, while *Thornton and Guza* [1983] reports values as large as $Q_b=0.6$ in shallow water. This is likely due to a combination of data processing and data collection methods. The semiautomated breaking detection algorithm employed in this study is designed to avoid false positives, but not false negatives, likely resulting in an underestimate of breaking counts. Further, the [*Young*, 1999] peak frequency is often slightly

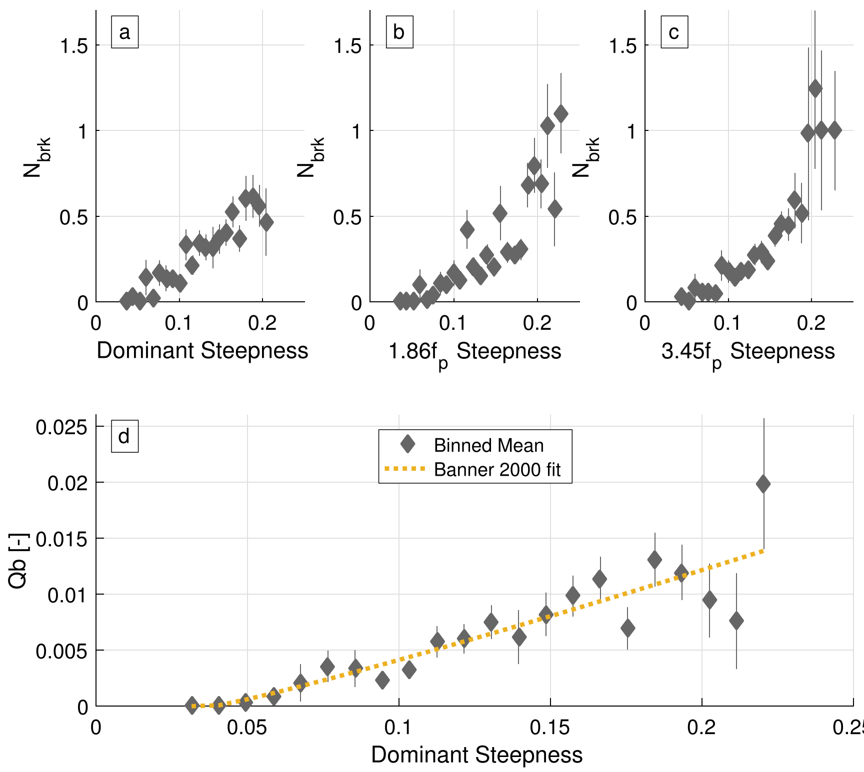

Figure 8. Wave breaking rate (number per 5 min) is bin averaged and plotted against steepness ($s=H_r k_r \tanh(k_r d)$) defined on scales relative to (a) f_p, (b) 1.86f_p, and (c) 3.45f_p. The *Banner et al.* [2000] model for breaking fraction in the dominant wave breaking scale is compared with binned means in Figure 8d.

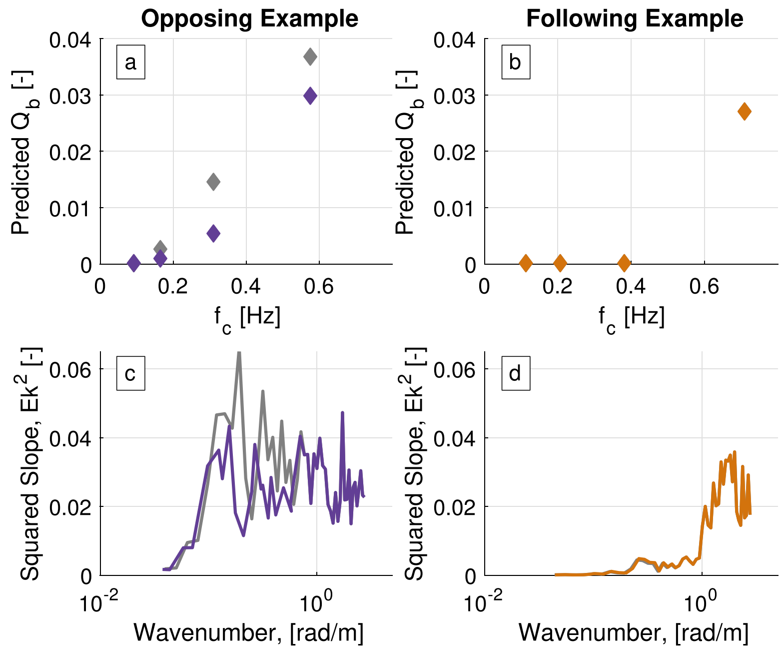

Figure 9. Example predictions of breaking fraction for each centered frequency bin for the *Filipot et al*. [2010] model for (a) an ebb case and (b) a flood case. Grey points show the prediction without the sheared wavenumber correction. Spectral squared slope examples are shown in Figures 9c and 9d.

above the spectral energy maximum, which may overestimate the number of waves in each 5 min burst, thus decreasing estimates of Q_b. While these two artifacts may reconcile the difference between this study's measured breaking fractions and reported deep water breaking fractions, it is unlikely to account for the difference with shallow water breaking fractions which are an order of magnitude larger. Of course, the waves in this study are not in shallow water, but rather range from intermediate to deep water conditions.

Despite infrequently measured breaking, there is still an apparent lower limit, below which no breaking is observed, $H_s k_m / \tanh(k_m d) = 0.1$, or $\beta_r = 0.05$. This value is similar to the $Hk/2 = 0.055$ observed in *Banner et al*. [2000] as a lower threshold on wave breaking steepness in deep water.

3.3. *Filipot et al*. [2010] Comparison With N_{brk}

In addition to the bulk parameter models, these observations can be applied as quasi-spectral estimates of wave breaking to provide an evaluation of the *Filipot et al*. [2010] model. Examples are shown in Figure 9 for opposing waves and currents (Figure 9a), and following waves and currents (Figure 9b). Breaking on following currents was primarily predicted for the shortest wave scale, 3.45 f_p, while the shear correction mostly affects frequencies in the middle of the spectrum. Therefore, breaking rates on floods are not affected by the distinction between $U_{surface}$ and U_{eff}. Predicted breaking rates on ebbs, (opposing waves/currents), however, are greatly affected by this shear correction, as shown in Figure 9a. This is because there are notable changes to spectral steepness in Figure 9c that are caused by the adjustment to U_{eff}. In this case, failure to correct for the sheared current results in over prediction of breaking fraction by about 50%. In part, this is due to breaking occurring in frequency bands more effected by the sheared currents, ($0.1 < f < 0.4$, Figure 4b), and that the predictions of Q_b grow quickly with steepness, such that the prediction is sensitive to small changes to the estimated wavenumber.

Extending this model to the entire data set, the total number breakers per wave spectrum predicted by the *Filipot et al*. [2010] model are compared with measured breaking data in Figure 10a. Since *Filipot et al*. [2010] subdivides a spectrum into four wave scales, the breaking fraction for each wave scale is multiplied by the estimated number of waves, $f_c \tau$, and summed together for an estimate of the total number of breakers per burst interval. This allows comparison between the model and the measured data, but in doing so effectively integrates over the spectrum, obscuring the model's predictions of scale. The model is well-

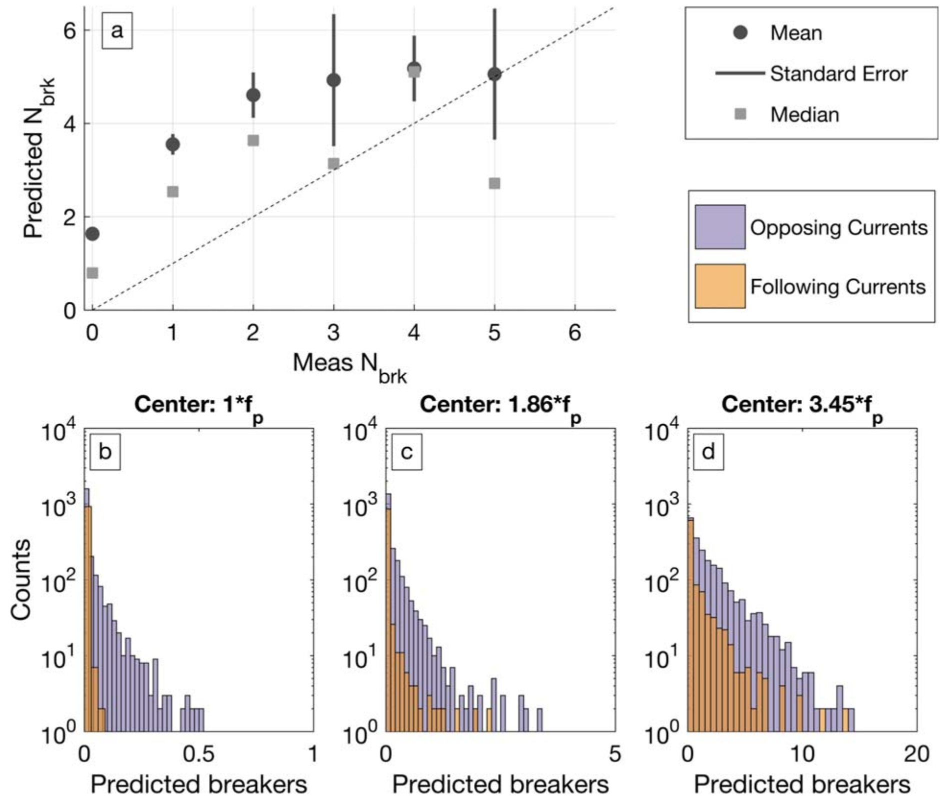

Figure 10. (a) Bin averaged predictions of the total number of breaking waves using the *Filipot et al*. [2010] model are compared with breaking measurements. Histograms of the predicted breakers per frequency bin (i.e., wave scale) are shown in Figures 10(b), 10(c), and 10(d), colored by opposing or following current direction.

correlated with the observations; however, the model over predicts breaking (i.e., mean of the residuals is $\langle N_{model} - N_{meas} \rangle = 1.6$). This is especially apparent in the $N_{brk} < 3$ range, which accounts for over 90% of the measured data. Most of the breaking predicted in the *Filipot et al*. [2010] model is in the shortest wave scale, 3.45 f_p (Figure 10d). No breaking is predicted at frequencies less than the spectral peak (i.e., the longest wave scale) and thus that histogram is excluded from Figure 10. Of course, this particular result is sensitive to the definition of spectral peak and the spectral shapes within this data set; applying the *Filipot et al*. [2010] model to other data sets might predict breaking at these long scales.

There is a general separation of scales between cases of following and opposing currents. On following currents, the *Filipot et al*. [2010] model primarily predicts breaking in the shortest wave scale. On opposing currents, the model again predicts that the shortest wave scale also has the most breaking, but the longer scales have proportionately much more breaking activity.

4. Discussion

The *Chawla and Kirby* [2002] model performs well, given only one free fitting parameter, γ. The model was modified from a shallow water form to include currents, which often shift breaking to intermediate depths. It is interesting to note that this model still performs well in this study, where approximately 80% of the data were in deep water (defined $d/L > 0.5$). This supports the use of a universal (unified, finite-depth) model for wave breaking, such as *Filipot et al*. [2010].

It is not surprising that the *Filipot et al*. [2010] over predicts wave breaking, given first that our measured breaking rates are likely underestimated due to type-2 error, and second, that we may be overestimating steepness on the ebbs (majority of data) due to the assumption of linear dispersion with a first order adjustment to the currents. In particular, [*Kirby and Chen*, 1989] made the assumption that $U/c \ll 1$, which is likely true for long waves in this study, but certainly not accurate in the short waves which often neared or

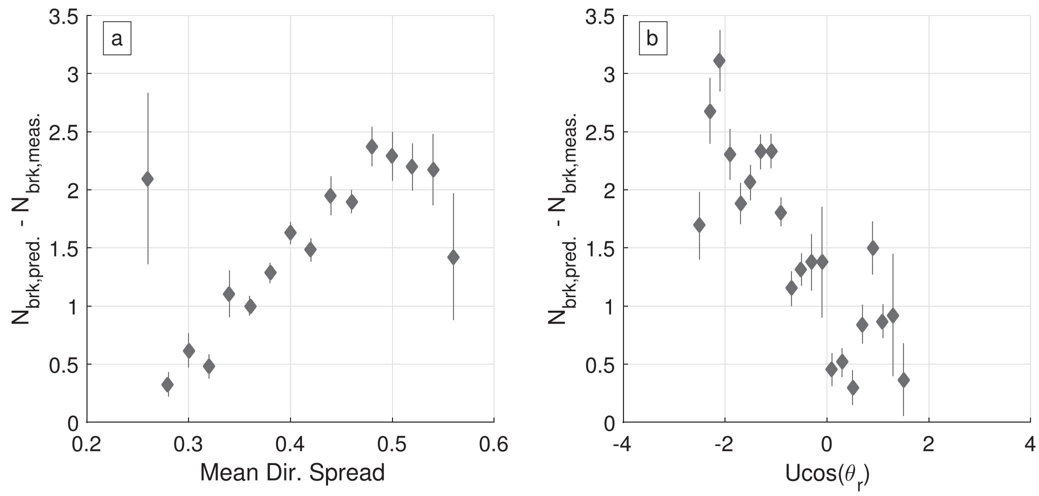

Figure 11. (a) Wave breaking count residuals from the *Filipot et al*. [2010] model, $N_{model} - N_{meas}$, are bin averaged and plotted against mean directional spread, and (b) the relative wave/current strength. Error bars show standard error.

reached blocking conditions on strong ebbs. Further, the majority of breaking predicted in the *Filipot et al*. [2010] model is in the higher frequency bands, where this effect would be strongest.

4.1. Directionality

A number of studies have suggested that increased directional spread, $\Delta\theta$ decreases breaking rates or probabilities [*Banner et al*., 2002; *Gemmrich*, 2010; *Gemmrich et al*., 2013; *Schwendeman and Thomson*, 2015], or stated differently, that unidirectional waves are more likely to break. Further, *Filipot et al*. [2010] briefly discusses the importance of directional spread, but did not have directional data available for comparison. Figure 11a supports this hypothesis by showing a positive trend with averaged *Filipot et al*. [2010] model residuals ($N_{model} - N_{meas}$) and energy averaged directional spread, defined by

$$(\Delta\theta)_m = \frac{\int E(f)(\Delta\theta)df}{\int E(f)df}, \tag{16}$$

with spread estimated from the Kuik parameters $\Delta\theta(f) = \sqrt{\left(1 - \sqrt{a_2(f)^2 + b_2(f)^2}\right)/2}$ [*Kuik et al*., 1988; *Herbers et al*., 2012]. At relatively low directional spreads ($\Delta\theta_m = 0.3$), the model does well in the mean, only slightly over predicting the breaking (mean residuals are 0.5), while as directional spread increases the model predicts much more breaking than was observed (mean residuals of ~ 2 at $\Delta\theta = 0.5$). This suggests that for the same steepness, waves with narrower directional spreading are more likely to break.

Residuals also appear to have a negative trend with the apparent current strength, $U\cos(\theta_r)$, as shown in Figure 11b. While it is possible that the two effects are related, as opposing currents cause refraction, which may lead to increased directional spread, there is no correlation or mean trend between $U\cos(\theta_r)$ and $\Delta\theta_m$. Two effects could then explain the correlation of $U\cos(\theta_r)$ and residuals. As suggested in lab study of *Yao and Wu* [2005], vertical shear $\partial U/\partial z$ could have a slight effect on wave breaking steepness, with waves breaking at steeper values for negative shear (as was seen on opposing currents, Figure 3). Therefore, less breaking would occur on large negative $U\cos(\theta_r)$; however, more breaking would be predicted based on a constant breaking threshold $\tilde{\beta}$. The other possibility is that our measurements still over predict steepness values on ebbs, even after the shear correction, due to the assumption of linear, first-order shear dispersion, the assumed mean velocity profiles, or other factors. Without direct measurement of wavenumber, it is difficult to distinguish between the two effects.

4.2. Interpretation of the Limiting Steepness, γ

The range of steepness parameters that best fit the breaking data ($\gamma = 0.96, 0.65$, Figure 7, and Table 2) is much larger than the maximum bulk steepness values observed in the data ($\gamma = 0.4$, Figure 6). This discrepancy can be attributed to an assumption inherent in the model, that as the local steepness approaches the value of the breaking parameter, the breaking fraction must approach 0.5 (i.e., every other wave is breaking). This is a logical assumption for the surf zone (where the Rayleigh distribution-based breaking models were developed) where waves tend to reach breaking saturation as they approach the shoreline. However, mean breaking fractions for the steepest observed waves in this study were approximately 2%, clearly far from saturation. The result is a larger best fit breaking parameter than observed limiting steepness (e.g., Figure 6). This discrepancy in breaking fraction highlights some of the difficulties in a unified deep and shallow water wave breaking theory. Breaking in the two regimes have differing characteristics, which can be difficult to reconcile under the same limitations. For example, the relation of whitecap coverage to wind speed in deep water can be stronger than to wave statistics [*Schwendeman and Thomson*, 2015], where in shallow water breaking is primarily controlled by bathymetry.

4.3. Strong Horizontal Current Gradients at Fronts

The images of flooding and ebbing fronts shown in Figure 5 highlight an important aspect of wave breaking that has not yet been discussed here. Fronts were commonly seen at the Mouth of the Columbia River, and these were visually observed to be regions of intense breaking. They were also regions where the horizontal gradient in currents was large, both on ebbs when the (relatively) quiescent ocean water meets the outflowing river current, and on flooding fronts where the incoming tide is opposed by river currents. For both of these scenarios, the adverse gradient felt by the waves would require a rapid increase in wave steepness, often to an asymptote, as discussed in *Babanin et al*. [2011] and *van der Westhuysen* [2012]. Characterization of the spatial gradients from buoy point measurements (drifters) was not possible, because the buoys remain trapped in the fronts and the horizontal gradients are not quantified. Further, only a select number of examples included visual confirmation from a shipboard observer. Still, the drifters in fronts generally measured much higher breaking rates than the mean wave steepness in the area. This may contribute to the high variability in mean breaking fraction in the steepness range, $0.15 < H_s k_m / \tanh(k_m d) < 0.25$, as bulk wave parameters likely do not capture other potential effects leading to breaking at fronts, such as single and double reflection [*Trulsen and Mei*, 1993; *Rousseaux et al*., 2008, 2010], nonlinear interactions [*Liu et al*., 1990], and sideband growth [*Chawla and Kirby*, 2002; *Babanin et al*., 2011].

4.4. Implications for Spectral Wave Modeling

These results highlight the importance of including the vertical distribution of currents in spectral wave modeling. For example, using only surface currents in tidal inlets where vertical shear is expected could result in over estimates of steepness, and incorrect blocking frequencies resulting in overly large wave heights and incorrectly distributed wave dissipation. On flooding (following) currents, wave steepness may be understated, due to overestimations of the following current. While the changes in steepness are relatively small (<20%), they can result in large differences in breaking rates due to the shape of the breaking fraction functions.

This study focuses on breaking fractions, an underlying assumption in many dissipation models, rather than the dissipation itself. However, the poor agreement of the *Battjes and Janssen* [1978] model with the measured data casts doubt on dissipation models which include $Q_{b,BJ78}$ (e.g., *Ris and Holthuijsen* [1996] dissipation model for waves/currents). The success of *Chawla and Kirby* [2002] in fitting observed breaking data, and the relative success of the *Filipot et al*. [2010] breaking model give credence to modifications to the shallow water-based dissipation models. Still, this study only quantifies and compares the wave breaking statistics, and not the underlying estimated wave dissipation. Further, the success of the *Filipot et al*. [2010] provides a basis for a universal wave breaking parameterization applicable in deep and shallow water.

5. Conclusions

Measurements of waves and currents were collected at the Mouth of the Columbia River between May and September 2013. Profiles of velocity in the top 25 m of the water column were used to refine the calculation of wavenumber, helping prevent the otherwise erroneously large estimates of wave steepness on opposing currents. We find the spectral correction to wave number is necessary in analysis of bulk steepness. The range of all bulk steepness values fall below $\gamma = 0.4$, consistent with other studies.

Wave-breaking models based on a weighted Rayleigh distribution of breaking wave heights do well to explain the trends in measured wave breaking fractions. These models are based on a finite-depth steepness, applicable to intermediate depth environments where wave breaking is often observed at river inlets. A quasi-spectral model also compares well with measured wave breaking. Measurements of directional spread indicate a relation to wave breaking as well, qualitatively consistent with previous deep water wave dissipation parameterizations.

In some ways, it is remarkable that linear methods for wave breaking work so well in these environments. The key to the success of these models in representing the field data is likely the statistical nature of the approach. In short, the probability of breaking is captured by the bulk parameters of the waves, with proper adjustment for sheared currents and finite-depths, but the details of the breaking process (and the inherent nonlinearity) are yet to be revealed.

Appendix A: Velocity Binning and U_{eff} Sensitivity

Twenty bins of relative surface velocity, $U\cos(\theta_r)$, spaced at 0.29 m s^{-1} were used to create the mean velocity profiles in Figure 3. Of the 5293 5 min bursts collected, 1198 5 min averaged velocity profiles were collected (22% of the data). The validity of using the bin-averaged velocity profiles in the top 25 m of the water column to estimate mean wavenumber was tested in the following ways.

A.1. Data Denial

A data denial study showed that using binned, mean profiles of velocity estimated similar mean wave numbers, k_m, to those estimated using the measured profiles. Mean profiles were calculated with 85% of the measured profiles (selected with a random number generator), and the remaining 15% were used for cross-validation. Here we will use $k_{m,meas.}$ for mean wavenumbers estimated using measured profiles, and $k_{m,mean}$ for mean wavenumbers estimated with the bin-averaged velocity profiles. Both the training data used to create the mean profiles, and the cross-validation set showed narrow Gaussian-shaped histograms of residuals, $k_{m,meas.} - k_{m,mean}$. The normalized residuals had means near zero, (-6.6×10^{-4} and 2.4×10^{-4} for training and cross-validation sets, respectively) and small variance (3.0×10^{-4} and 3.9×10^{-4} for training and cross-validation sets, respectively).

A.2. Profile Depth Limitations

Many of the measured velocity profiles did not extend to the full water depth. However, extrapolations of measured velocity profiles to include velocities below 25 m water depth did not significantly affect estimates of mean wavenumber, k_m. Velocity profiles were fit with an exponential decay model to extrapolate velocities below 25 m. These extended profiles were then used to estimate mean wavenumber where the measured profile did not extend the full water column. All the extrapolated profiles were less than 0.1% different from the profiles using measured velocity profiles ($|k_{m,extrap}/k_{m,meas.} - 1| < 10^{-3}$). This is likely because velocity shear is greatest near the surface, and because the surface velocities are weighted larger in the estimation of U_{eff} (equation (10)).

Acknowledgments
SWIFT data are available at http://www.apl.washington.edu/swift. Thanks to the field engineers, Joe Talbert and Alex de Klerk, and those who helped with data collection, including Cigdem Akan, Chris Bassett, Adam Brown, Walter Deppe, Adam Keen, Saeed Moghami, Curis Rusch, the crews of the R/V Oceanus, the R/V Pt. Sur, and the F/V Westwind. Adam Keen helped to develop the original image processing to detect breakers. Cigdem Akan helped to prepare the bathymetry data. Thanks to Tim Janssen and Alex Horner-Devine for helpful feedback. Thanks to the EFM group at UW for support and helpful suggestions. This work was supported by the Office of Naval Research, as part of the Data Assimilation and Remote Sensing for Littoral Applications (DARLA) project and in coordination with the Rivers and Inlets (RIVET) program.

References

Babanin, A. V., H.-H. Hwung, I. Shugan, A. Roland, A. van der Westhuysen, A. Chawla, and C. Gautier (2011), Nonlinear waves on collinear currents with horizontal velocity gradient, in *Proceedings of the 12th International Workshop on Wave Hindcasting and Forecasting and 3rd Coastal Hazards Symposium*, vol. 4, Big Island, Hawaii, 30 Oct.–Nov. [Available at www.waveworkshop.org/12thWaves/index.htm.]

Banner, M., J. Gemmrich, and D. Farmer (2002), Multiscale measurements of ocean wave breaking probability, *J. Phys. Oceanogr.*, *32*, 3364–3375.

Banner, M. L., A. V. Babanin, and I. Young (2000), Breaking probability for dominant waves on the sea surface, *J. Phys. Oceanogr.*, *30*, 3145–3160.

Battjes, J. A., and J. P. F. M. Janssen (1978), Energy loss and set-up due to breaking of random waves, in *Proceedings of 16th International Conference on Coastal Engineering*, pp. 569–587, Am. Soc. of Civ. Eng., New York.

Booij, N., R. C. Ris, and L. H. Holthuijsen (1999), A third-generation wave model for coastal regions: 1. Model description and validation, *J. Geophys. Res.*, *104*(C4), 7649–7666.

Callaghan, A., G. de Leeuw, L. Cohen, and C. D. O'Dowd (2008), Relationship of oceanic whitecap coverage to wind speed and wind history, *Geophys. Res. Lett.*, *35*, L23609, doi:10.1029/2008GL036165.

Campana, J., E. J. Terrill, and T. de Paolo (2016), The development of an inversion technique to extract vertical current profiles from x-band radar observations, *J. Atmos. Oceanic Technol.*, *33*(9), 2015–2028.

Chawla, A., and J. T. Kirby (2002), Monochromatic and random wave breaking at blocking points, *J. Geophys. Res.*, *107*(C7), doi:10.1029/2001JC001042.

Chen, J. L., T. J. Hsu, F. Shi, B. Raubenheimer, and S. Elgar (2015), Hydrodynamic and sediment transport modeling of new river inlet (NC) under the interaction of tides and waves, *J. Geophys. Res. Oceans*, *120*, 4028–4047, doi:10.1002/2014JC010425.

Craig, P. D., and M. L. Banner (1994), Modeling wave-enhanced turbulence in the ocean surface layer, *J. Phys. Oceanogr.*, *24*, 2546–2559.

Dodet, G., X. Bertin, N. Bruneau, A. B. Fortunato, A. Nahon, and A. Roland (2013), Wave-current interactions in a wave-dominated tidal inlet, *J. Geophys. Res. Oceans*, *118*, 1587–1605, doi:10.1002/jgrc.20146.

Drazen, D., W. K. Melville, and L. Lenain (2008), Inertial scaling of dissipation in unsteady breaking waves, *J. Fluid Mech.*, *611*, 307–332.

Filipot, J. F., F. Ardhuin, and A. V. Babanin (2010), A unified deep-to-shallow water wave-breaking probability parameterization, *J. Geophys. Res.*, *115*, C04022, doi:10.1029/2009JC005448.

Gelfenbaum, G., D. Finlayson, P. Dartnell, E. Carlson, and A. Stevens (2015), Bathymetry and backscatter from 2013 interforometric swath bathymetry systems survey of Columbia River Mouth, Oregon and Washington, U.S. Geological Survey data release. [Available at https://doi.org/10.5066/F7T72FHB.]

Gemmrich, J. (2010), Strong turbulence in the wave crest region, *J. Phys. Oceanogr.*, *40*, 583–595.

Gemmrich, J., C. J. Zappa, M. L. Banner, and R. P. Morison (2013), Wave breaking in developing and mature seas, *J. Geophys. Res. Oceans*, *118*, 4542–4552, doi:10.1002/jgrc.20334.

Gemmrich, J. R., M. L. Banner, and C. Garrett (2008), Spectrally resolved energy dissipation rate and momentum flux of breaking waves, *J. Phys. Oceanogr.*, *38*, 1296–1312.

Gerbi, G. P., R. J. Chant, and J. L. Wilkin (2013), Breaking surface wave effects on river plume dynamics during upwelling-favorable winds, *J. Phys. Oceanogr.*, *43*(9), 1959–1980, doi:10.1175/JPO-D-12-0185.1.

Gonzalez, F. I., and C. L. Rosenfeld (1984), Slar and in situ observations of ocean swell modification by currents and bathymetry and the Columbia River entrance, *IEEE Trans. Geosci. Remote Sens.*, *GE-22*(6), 598–603.

Hansen, J. E., T. T. Janssen, B. Raubenheimer, F. Shi, P. L. Barnard, and I. S. Jones (2014), Observations of surfzone alongshore pressure gradients onshore of an ebb-tidal delta, *Coastal Eng.*, *91*, 251–260.

Herbers, T. H. C., and T. T. Janssen (2016), Lagrangian surface wave motion and stokes drift fluctuations, *J. Phys. Oceanogr.*, *46*(4), 1009–1021, doi:10.1175/JPO-D-15-0129.1.

Herbers, T. H. C., P. F. Jessen, T. T. Janssen, D. B. Colbert, and J. H. MacMahan (2012), Observing ocean surface waves with GPS-tracked buoys, *J. Atmos. Oceanic Technol.*, *29*, 944–959.

Hopkins, J., S. Elgar, and B. Raubenheimer (2015), Observations and model simulations of wave-current interaction on the inner shelf, *J. Geophys. Res. Oceans*, *121*, 198–208, doi:10.1002/2015JC010788.

Janssen, T. T., and J. Battjes (2007), A note on wave energy dissipation over steep beaches, *Coastal Eng.*, *54*(9), 711–716, doi:10.1016/j.coastaleng.2007.05.006.

Kang, K., and D. D. Iorio (2006), Depth-and current-induced effects on wave propagation into the Altamaha river estuary, Georgia, *Estuarine Coastal Shelf Sci.*, *66*, 395–408.

Kassem, S., and H. T. Ozkan-Haller (2012), Forecasting the wave-current interactions at the Mouth of the Columbia River, or, USA, in *33rd International Conference on Coastal Engineering*, Santander, Spain. [Available at http://dx.doi.org/10.9753/icce.v33.waves.53.]

Kirby, J. T., and T. Chen (1989), Surface waves on vertically sheared flows: Approximate dispersion relations, *J. Geophys. Res.*, *94*(C1), 1013–1027.

Kleiss, J. M., and W. K. Melville (2010), Observations of wave breaking kinematics in fetch-limited seas, *J. Phys. Oceanogr.*, *40*(12), 2575–2604, doi:10.1175/2010JPO4383.1.

Kuik, A. J., G. P. V. Vledder, and L. H. Holthuijsen (1988), A method for the routine analysis of pitch-and-roll buoy wave data, *J. Phys. Oceanogr.*, *18*, 1020–1035.

Lagarias, J. C., J. A. Reeds, M. H. Wright, and P. E. Wright (1998), Convergence properties of the Nelder-Mead simplex method in low dimensions, *SIAM J. Optim.*, *9*(1), 112–147.

Liu, P., M. W. Dingemans, and J. K. Kostense (1990), Long-wave generation due to the refraction of short-wave groups over a shear current, *J. Phys. Oceanogr.*, *20*, 53–59.

Longuet-Higgins, M. S., and R. W. Stewart (1962), Radiation stress and mass transport in gravity waves, with application to 'surf beats', *J. Fluid Mech.*, *13*(4), 481–504, doi:10.1017/S0022112062000877.

Lund, B., H. C. Graber, H. Tamura, C. O. Collins, and S. M. Varlamov (2015), A new technique for the retrieval of near-surface vertical current shear from marine x-band radar images, *J. Geophys. Res. Oceans*, *120*, 8466–8486, doi:10.1002/2015JC010961.

Masson, D. (1996), A case study of wave-current interaction in a strong tidal current, *J. Phys. Oceanogr.*, *26*, 359–372.

Mendez, G. M. D., M. C. Haller, B. Raubenheimer, S. Elgar, and D. A. Honegger (2015), Radar remote sensing estimates of waves and wave forcing at a tidal inlet, *J. Atmos. Oceanic Technol.*, *32*, 842–854.

Miche, A. (1944), Mouvements ondulatoires de la mer en profondeur croissante ou d é croissante. forme limite de la houle lors de son d é ferlement. application aux digues maritimes. deuxi è me partie. mouvements ondulatoires p é riodiques en profondeur r é guli è rement d é croissante., *Ann. Ponts et Chauss é es*, *114*, 369–406.

Monahan, E. C. (1971), Oceanic whitecaps, *J. Phys. Oceanogr.*, *1*, 139–144.

Monahan, E. C., and I. O. Muircheartajgh (1980), Optimal power-law description of oceanic whitecap coverage dependence on wind speed, *J. Phys. Oceanogr.*, *10*, 2094–2099.

Olabarrietta, M., J. C. Warner, and N. Kumar (2011), Wave-current interaction in Willapa bay, *J. Geophys. Res. Oceans*, *116*, C12014, doi:10.1029/2011JC007387.

Olabarrieta, M., W. R. Geyer, and N. Kumar (2014), The role of morphology and wave-current interaction at tidal inlets: An idealized modeling analysis, *J. Geophys. Res. Oceans*, *119*, 8818–8837, doi:10.1002/2014JC010191.

Pearman, D., T. H. C. Herbers, T. T. Janssen, H. D. van Ettinger, and S. A. McIntyre (2014), Drifter observations of the effects of shoals and tidal-currents on wave evolution in San Francisco bight, *Cont. Shelf Res.*, *91*, 109–119.

Rascle, N., and F. Ardhuin (2009), Drift and mixing under the ocean surface revisited: Stratified conditions and model-data comparisons, *J. Geophys. Res. Oceans*, *114*, C02016, doi:10.1029/2007JC004466.

Raubenheimer, B., R. T. Guza, and S. Elgar (1996), Wave transformation across the inner surf zone, *J. Geophys. Res.*, *101*(C10), 25,589–25,597.

Ris, R. C., and L. H. Holthuijsen (1996), Spectral modelling of current induced wave-blocking, in *Proceedings of the 25th International Conference on Coastal Engineering*, pp. 1247–1254, Am. Soc. of Civ. Eng., New York.

Rousseaux, G., C. Mathis, P. Maissa, T. G. Philbin, and U. Leonhardt (2008), Observation of negative-frequency waves in a water tank: A classical analogue to the hawking effect?, *New J. Phys.*, *10*(5), 053015, doi:10.1088/1367-2630/10/5/053015.

Rousseaux, G., P. Maissa, C. Mathis, P. Coullet, T. G. Philbin, and U. Leonhardt (2010), Horizon effects with surface waves on moving water, *New J. Phys.*, *12*(9), 095018, doi:10.1088/1367-2630/12/9/095018.

Rusch, C., J. Thomson, S. Zippel, and M. Schwendeman (2014), Video recognition of breaking waves, *Oceans-St. John's*, pp. 1–6, IEEE, Piscataway, N. J., doi:10.1109/OCEANS.2014.7002994.

Schwendeman, M., and J. Thomson (2015), Observations of whitecap coverage and the relation to wind stress, wave slope, and turbulent dissipation, *J. Geophys. Res. Oceans*, *120*, 8346–8363, doi:10.1002/2015JC011196.

Stewart, R. H., and J. W. Joy (1974), Hf radio measurements of surface currents, *Deep Sea Res. Oceanogr. Abstr.*, *21*, 1039–1049.

Terray, E., M. Donelan, Y. Agrawal, W. Drennan, K. Kahma, A. Williams, P. Hwang, and S. Kitaigorodskii (1996), Estimates of kinetic energy dissipation under breaking waves, *J. Phys. Oceanogr.*, *26*, 792–807.

Thomson, J. (2012), Wave breaking dissipation observed with SWIFT drifters, *J. Atmos. Oceanic Technol.*, *29*(12), 1866–1882, doi:10.1175/JTECH-D-12-00018.1.

Thomson, J., and A. Jessup (2009), A Fourier-based method for the distribution of breaking crests from video observations, *J. Atmos. Oceanic Technol.*, *26*(8), 1663–1671.

Thomson, J., A. R. Horner-Devine, S. Zippel, C. Rusch, and W. Geyer (2014), Wave breaking turbulence at the offshore front of the Columbia River plume, *Geophys. Res. Lett.*, *41*, 8987–8993, doi:10.1002/2014GL062274.

Thornton, E. B., and R. T. Guza (1983), Transformation of wave height distribution, *J. Geophys. Res.*, *88*(C10), 5925–5938.

Trulsen, K., and C. C. Mei (1993), Double reflection of capillary/gravity waves by a non-uniform current: A boundary-layer theory, *J. Fluid Mech.*, *251*, 239–271.

van der Westhuysen, A. J. (2012), Spectral modeling of wave dissipation on negative current gradients, *Coastal Eng.*, *68*, 17–30, doi:10.1016/j.coastaleng.2012.05.001.

Yao, A., and C. H. Wu (2005), Incipient breaking of unsteady waves on sheared currents, *Phys. Fluids*, *17*(8), 082104, doi:10.1063/1.2000276.

Young, I. (1999), *Wind Generated Ocean Waves*, Elsevier Ocean Engineering Book Series, Elsevier, New York.